Enhanced nucleate boiling using a reduced graphene oxide-coated micropillar

Geehong Choi[a], Dong Il Shim[a], Donghwi Lee[a], Beom Seok Kim[b], Hyung Hee Cho[a,*]

[a] *Department of Mechanical Engineering, Yonsei University, 03722 Seoul, Republic of Korea*
[b] *National Fusion Research Institute, 34133 Daejon, Republic of Korea*

ARTICLE INFO

ABSTRACT

Critical heat flux (CHF) enhancement is necessary in order to ensure a high operating limit for two-phase cooling applications. As the boiling is developed, formation of vapor film layer becomes vigorous, which causes CHF. Here, a graphene-coated micropillar structure (GMS) is proposed in order to enhance boiling heat transfer by suppressing vapor film formation on the surface. The GMS is designed to separate the bubble nucleation region from the liquid supply region in order to enhance CHF. By controlling the height of the micropillar, we obtained a structure in which the rGO layer is coated at the top of the micropillar array with high aspect ratio of the micropillar. In particular, the GMS consists of a reduced graphene oxide (rGO) porous mesh layer and a micropillar array layer. The rGO porous structure facilitated bubble nucleation by providing a suitably sized cavity. The micropillar array, which has excellent wicking performance, is located below the rGO porous layer in order to provide a capillary pumping to the vapor bubbles. Consequently, the GMS provides a significantly improved heat transfer coefficient and CHF of 288% and 152%, respectively, compared to the plain surface.

1. Introduction

Boiling is an effective cooling technology that can maintain stable thermal conditions by absorbing latent heat. In boiling heat transfer, the heat transfer coefficient (HTC) and critical heat flux (CHF) are the main factors that represent boiling performance. In particular, CHF is the maximum heat dissipation capacity for cooling through nucleate boiling. There are various theoretical models to describe CHF. [1] The hydrodynamic instability model explained that CHF occurs due to the instability between vapor and liquid flowing in different directions [2]. Based on bubble visualization, the researchers observed that the bubbles coalesce with each other before departure, forming a mushroom shape. Haramura and Katto proposed that the CHF occurs due to the dry-out of the macro-liquid layer under the mushrooms [3]. Later, as the bubble visualization technology developed, the macro-liquid layer dry-out model was connected to a micro-liquid layer dry-out model [4]. Another cause of the CHF generation is the bubble interaction. This model implies that CHF occurs by blocking the liquid flow path to the surface when the bubbles are tightly distributed on the heating surface [5]. Comprehensively, the various theoretical models explained that CHF is occurred when the liquid supply is blocked by vigorous bubble formation. The blockage of liquid supply causes the heating surface to be covered with vapor film. The vapor film with low thermal

conductivity prevents heat dissipation from the heated surface and causes sharp increase of surface temperature [6]. Therefore, it is necessary to secure stable liquid supply in order to improve the CHF.

Research into boiling heat transfer has indicated that surface characteristics are important parameters related to CHF. The use of nanofluids is an efficient approach to improving the surface roughness and wettability of boiling surfaces [7–11]. The boiling surface that is used in a nanofluid boiling experiment has a nanoparticle-coated structure [12]. This structure presents an increased heat transfer area and increased roughness in order to provide many nucleation sites. In addition, surface wettability and capillary pumping are improved to increase the CHF. However, as the coating thickness increases, the increased thermal resistance effect reduces heat transfer performance [8,13]. In order to overcome this problem, graphene has recently been used as a nanofluid in boiling research because of its high thermal conductivity [14–17]. Its high thermal conductivity inhibits the formation of dry hot spots, while its porous structure improves the CHF by reducing the critical wavelength between vapor columns [14]. However, graphene exhibits low wetting, which limits its capacity to enhance the CHF in terms of liquid supply [18].

Liquid supply is an important factor related to the improvement of the CHF. The liquid supply to a dry spot can prevent vapor film coverage on a heating surface [19–22]. Wicking is a liquid propagation

---

* Corresponding author.
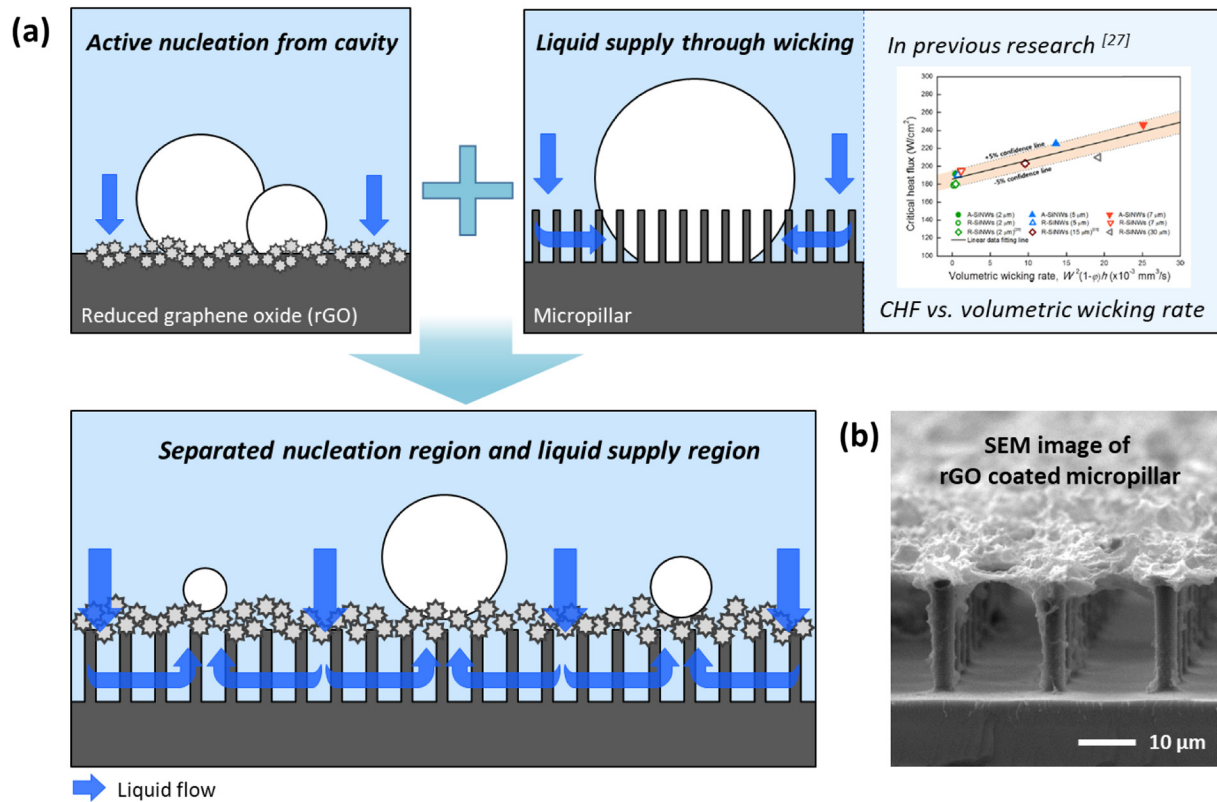*E-mail address:* hhcho@yonsei.ac.kr (H.H. Cho).

Fig. 1. Schematic of the boiling surface which has separated nucleation region and liquid supply region. (a) Schematic showing the combined active nucleation by reduced graphene oxide (rGO) and liquid supply through micropillar wicking structure, (b) SEM image of the rGO coated micropillar.

phenomenon that is driven by surface tension [23]. When the liquid is actively supplied through wicking around the bubbles, dry spot generation is suppressed and the CHF increases [4,24,25]. In this regard, various micro/nanostructures, such as micropillars, nanopillars, and nanowires, have been applied in order to improve the CHF performance by increasing the volumetric wicking rate [26–29]. These studies highlight the fact that a liquid supply provided through wicking is critical to enhancing the CHF.

In this paper, we propose a new structure that consists of a reduced graphene oxide (rGO) porous layer and a micropillars array as shown in Fig. 1. The effect of the graphene-coated micropillar structure (GMS) is investigated by pool boiling experiments with saturated temperature of liquid and ambient pressure conditions. The micropillar has a large aspect ratio of 5, which causes the rGO particles to form a layer near the micropillar tip. There is space for liquid supply between the micropillars under the rGO layer. In previous study, graphene and microstructure composite structure with small aspect ratio (< 2) was applied to boiling, and the rGO was entirely coated on microstructure array [30]. This structure could increase the heat transfer area by increasing the roughness, but it disturbs the liquid supply and traps bubbles like carbon nanotubes [31]. Therefore, the CHF performance was reduced rather than the micropillar surface. On the other hand, we fabricated the micropillar array layer and the rGO layer separately using the high aspect ratio of micropillar. The rGO mesh layer has opening between micropillar tips, and liquid flows through this opening to the micropillar layer. This rGO shape difference has the advantage of preventing bubble trap and enabling liquid supply. The porous rGO structure promotes bubble nucleation and the micropillar structure helps the supply of liquid to the boiling surface through wicking. In addition, the GMS is fabricated in such a way as to contain a separate bubble nucleation region (rGO) and liquid supply region (micropillar), thereby preventing vapor film formation and occurring effective heat transfer by decreasing interaction between the vapor flow and liquid flow. Our

aim is to determine whether the GMS is favorable for promoting bubble nucleation and capillary wicking, and thus for enhancing the CHF.

2. Material and methods

2.1. RTD sensor and thin film heater

The resistance temperature detector (RTD) sensor and thin-film heater is manufactured on a silicon wafer using MEMS [32]. A p-type silicon wafer (Boron-doped, (100) orientation, resistivity between 1 and 10 Ω, with a thickness of 550 μm) is used as the substrate. Before the fabrication process, the silicon wafer is cleaned for an hour with piranha solution (1:3 volume ratio of H_2O_2 and H_2SO_4), and for 10 min with a buffered oxide etchant (BOE) solution in order to remove the native oxide layer. After the cleaning process, an oxide layer is deposited by plasma-enhanced chemical vapor deposition (PECVD) for insulation. A photoresist (PR, GXR601) is coated on the wafer, and exposed to UV light with 4-wires RTD pattern mask. Pt is then deposited using an e-beam evaporator with a thickness of 100 nm. The 4-wires RTD patterning is developed by lift-off using acetone. The insulation layer is then added on top of the RTD pattern, and the layer electrically separates the RTD and heater layers. However, a particular area of the insulation layer is removed for electrode connection of the RTD sensor. Indium tin oxide is used as the thin-film heater with a heating area of 5×10 mm^2. The Au layer is deposited on the thin-film heater, and is connected with the copper bus-bar. There are five RTD sensors, spaced at a distance of 1.5 mm, and the circuit shape of RTD is serpentine in order to increase resistance to promote high temperature sensitivity. The RTD sensor is calibrated before the boiling experiment using a working-fluid temperature control based on the thermocouple in the boiling chamber. The Pt provides highly linear resistance with respect to temperature change, and the correlation has a high R^2 of over 0.999.

2.2. Micropillar fabrication

The micropillar used in the boiling experiment is fabricated on the backside of an RTD sensor and heater surface using the MEMS process. The micropillar has a circular cross section with a diameter of 4 μm, with a center-to-center pitch of 20 μm. The height of micropillar was changed to 5, 10, and 20 μm. The micropillar aspect ratio was controlled from 1.25 to 5. The surface for micropillar fabrication is cleaned with piranha and BOE solution, and coated with PR. After UV lithography, the silicon substrate is etched using deep reactive-ion etching (DRIE). The area that is covered with PR protects the silicon from the dry-etching process, and the silicon forms a micropillar structure. The remaining PR is removed using a plasma asher.

2.3. rGO synthesis

The rGO used in this study is synthesized using Hummer's method [33–35]. The synthesis method is divided into two stages. The first step is to oxidize the graphite and separate it into a graphene oxide (GO) layer, and the second step is to remove oxygen from the GO to form a graphene layer. This process contains oxidation and reduction reactions, thus the graphene synthesized by Hummer's method is referred to as a reduced graphene layer (rGO).

First, the graphite powder (1.5 g, 325 mesh, SP-1, Bay Carbon) is chemically oxidized using $K_2S_2O_8$ (2.5 g, 99.99% purity, Sigma-Aldrich), P_2O_5 (2.5 g, 99.99% purity, Sigma-Aldrich) and H_2SO_4 (12 mL, Duksan pure Chemicals). The mixed solution is heated to a temperature of 120 °C for 5 h using a hot plate. The pre-oxidized graphene is obtained by a previous process. Then, the powder is added to H_2SO_4 at a temperature of 10 °C, and $KMnO_4$ (15 g, Junsei Chemical Co. Ltd) is gradually added for 5 h. After this addition, the mixture is green, changing to red after oxidation reactions overnight. The mixture is diluted with 2500 mL water, and H_2O_2 (30 mL, Sigma-Aldrich) is added dropwise to the mixture. The GO solution is washed with DI water and HCl solution (1:10 of HCl and water, extra pure, Samchun Pure chemicals) to remove metal ions. Finally, the GO solution is reduced using Hydrazine monohydrate (3 μL) and ammonia solution (9 μL) at a temperature of 96 °C for 2 h. The concentration of the rGO solution is 0.0005% for the boiling experiments.

2.4. Boiling experiment system

The pool boiling experimental system consists of a boiling chamber that contains a transparent window, a DC power supply (200 V – 10 A, KSC Korea switching), a data-acquisition system (34970A, Agilent Technologies, and SCXI-1503, National Instruments), a condenser that is connected to a constant-temperature bath, and a high-speed camera (Speedsence M110, Dantec) as shown in Fig. 2 [36]. The temperature of the working fluid is maintained at the saturated temperature at atmospheric pressure. The pressure gauge and two K-type thermocouples are installed in the chamber. Before the boiling experiment, the working fluid is boiled for 2 h in order to remove gas that is dissolved in the liquid. There are transparent windows comprised of tempered glass on each of the four sidewalls of the chamber. An LED backlight (100 W) and high-speed camera are used to observe bubble characteristics and visualizations are recorded with a frequency of 2000 Hz. The boiling experiment is conducted by heat flux control, and the current is induced to the thin-film heater through a copper bus-bar. The wall temperature is measured using a RTD sensor. The silicon chip, which contains the thin-film heater and RTD sensor, is attached to a ceramic (Macerite-SP) plate, which exhibits a low thermal conductivity of 1.6 W/m·K. The ceramic plate and silicon chip are assembled in the test section in the chamber. The test section is made of polyether ether ketone (PEEK, k = 0.25 W/m·K). There is a silicone O-ring between the ceramic plate and test section in order to prevent leakage, and the two pieces are assembled using bolts.
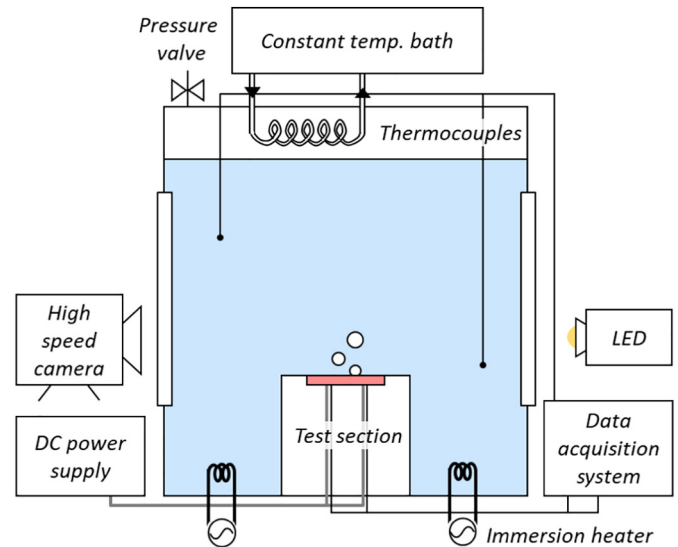

Fig. 2. Pool boiling experimental system.

2.5. rGO coating method

The rGO particles are coated on the surface using a nanofluid boiling method [14]. The rGO solution at 0.0005 wt% is added to the boiling chamber for use as a working fluid. The specimen to be used for rGO coating is installed in the boiling test section, and the process for the boiling experiment proceeds as described above. The heat flux was increased by 3 W/cm² to a point just before the CHF, and a coating time of 10 min was maintained at each heat flux condition. In this way, the rGO-coated surface was used in the boiling experiment with DI water as the working fluid.

2.6. Pool boiling data reduction

The heat flux (q'') is generated from the thin film heater and the value is calculated by induced current (I), voltage (V) and heating area (A).

$$q'' = \frac{I \times V}{A} \tag{1}$$

The wall temperature is evaluated by RTD sensors, but the sensors are located on the backside of the heat transfer surface. Thus, the wall temperature is calculated by the Fourier's law for 1D thermal conduction as shown in the below:

$$T_w = T_R - \frac{t}{k_{Si}} \cdot q'' \tag{2}$$

where T_w, T_R, t, and k_{Si} mean the wall temperature, temperature measured from RTD sensor, thickness of silicon substrate, and thermal conductivity of silicon, respectively. The boiling characteristic curve is obtained by using the calculated heat flux and wall temperature. The repeatability test of pool boiling experiments is presented in supporting information. Lastly, the heat transfer coefficient is investigated by the Newton's law for thermal convection as expressed as

$$h = q''/(T_w - T_f) \tag{3}$$

where h, and T_f mean heat transfer coefficient and temperature of working fluid. The uncertainty of data reduction is presented in the previous study, and the uncertainty of heat flux, wall superheat and heat transfer coefficient were 6.5%, 6.5%, and 9.2%, respectively [32,37].

3. Results and discussion

3.1. Design and fabrication of rGO-coated micropillar structure (GMS)

Fig. 1(a) shows the schematic of the rGO-coated micropillar structure (GMS) for boiling, which contains separate nucleation and liquid-supply regions. The GMS consists of an rGO coating layer and a micropillar array. The rGO layer has a porous structure with high thermal conductivity. This porous structure improves boiling heat transfer by enlarging the heat transfer area and providing a cavity in which bubbles can be generated. The liquid supply for bubble generation occurs through the micropillar layer. Wicking through a micropillar maintains the liquid-vapor mass balance in the phase-change interface by continuously supplying the liquid required for phase change in the rGO layer.

In addition, the GMS surface is divided into an rGO layer for bubble formation and a micropillar layer for liquid supply. For this reason, GMS can improve the critical heat flux by preventing vapor film formation at the phase-change interface. In order to realize a structure with a combined rGO and micropillar layer, difficulties related to the feasibility of fabrication must be addressed. The rGO must be selectively deposited on the tip of the micropillar in order to distinguish the bubble formation region from the liquid supply region. The rGO particles are deposited on the Si surface using the nanofluid boiling method, as mentioned in the experimental section. During the rGO coating experiment, the rGO particles are distributed in the micro-liquid layer between micropillars in the array. When the micro-liquid layer dries during the bubble-departure process, floating rGO particles that are in the form of nanofluids cannot escape into the bulk working fluid and adhere to the Si surface [12,38]. In particular, evaporation actively occurs at the liquid-vapor interface of the micro-liquid layer, and rGO particles are interconnected and attach to the tip of the micropillar, where there is the liquid-vapor interface. Fig. 1(b) shows the SEM image of the GMS.

Our GMS fabrication strategy allows control of the liquid-vapor interface position where rGO is deposited by controlling the height of the micropillar. The micropillar diameter and center to center pitch are maintained to 4 μm and 20 μm, respectively. The micropillar height is changed to 5, 10, and 20 μm, while its geometric range is set to be the dominant region of the capillary force caused by the surface tension rather than the friction force caused by the viscosity [39]. Fig. 3 shows

the GMS shapes according to the different micropillar heights. As boiling develops, the thickness of the micro-liquid layer between micropillars gradually decreases. In this process, the rGO layer that adheres to the tip of the micropillar at heights of 5 and 10 μm is gradually lowered and attached to the pillar side. On the other hand, in the case of the micropillar surface with a large aspect ratio (20 μm height), the rGO layer did not fall down to the side of the pillar, but adjacent rGOs were connected to each other. This orchard-like structure can be used to separate the rGO layer for bubble nucleation from the micropillar layer for liquid supply.

Fig. 4(a)–(c) show SEM images of the rGO-coated plain and rGO-coated micropillar surfaces obtained from the boiling experiments. Fig. 4(a) contains SEM images of a bare-Si plain surface, a cross section view of the rGO-coated plain surface, and a top view of the rGO-coated plain surface. The rGO particles begin to grow at a particular position, and the starting points are randomly distributed. The adjacent rGO islands are connected to each other. On the other hand, the shape of the rGO coating on the micropillar surface is different to that on the plain surface. Fig. 4(b) is the SEM images of micropillar surface before rGO coating, and Fig. 4(c) is the SEM images of micropillar surface after rGO coating. The rGO deposition on the micropillar surface begins at the micropillar tip, and the adjacent rGO islands are connected in a mesh form, leaving an empty space (dark gray region in the top view of Fig. 4(b)). The micropillar section has very low thermal resistance ($R_{thermal} \sim L/k$) due to its very short length (20 μm) and high thermal conductivity ($k_{Si} \sim 140$ W/m·K). The thermal resistance of the micropillar conduction is one order of magnitude lower than the thermal resistance generated by boiling convection. Therefore, the rGO layer maintains a superheating condition similar to the heating surface temperature (the base surface of the micropillar), and bubble nucleation becomes possible at the rGO layer. Below the rGO layer is the micropillar layer that supplies liquid to the bubbles through wicking. This micropillar layer makes a gap between the heating surface and the bubble by remaining in the liquid form [40]. Thus, the liquid is directly supplied to the heating surface to cool it down, and the surface overheating caused by the low thermal conductivity of the vapor may be suppressed.

The GMS surface exhibits an improved wicking performance compared to other micro/nano wicking structures [27,41]. Fig. 5 shows the contact angle and wicking length over time, with the wicking rate given by the slope of the graph [23]. Graphene is a carbon-based, nonpolar
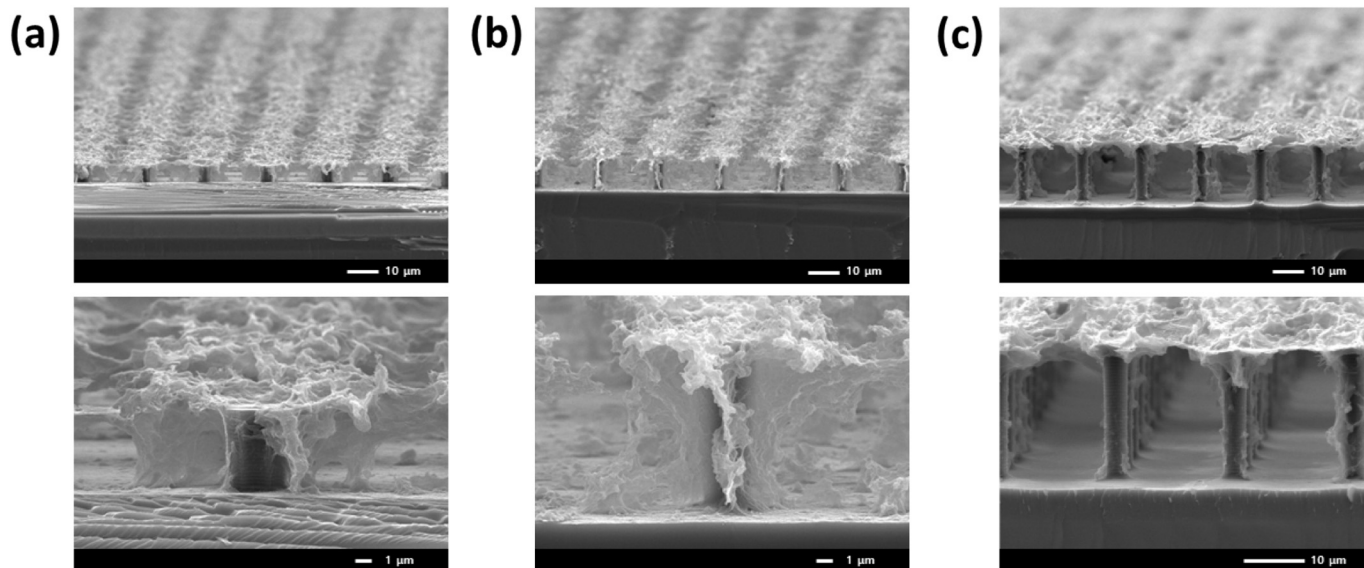

Fig. 3. Reduced graphene oxide (RGO) coating foam according to aspect ratio of micropillar. Micropillar with a height of (a) 5 μm, (b) 10 μm, (c) 20 μm. The diamteter of micropillar is 4 μm, and the center to centor pitch is 20 μm.
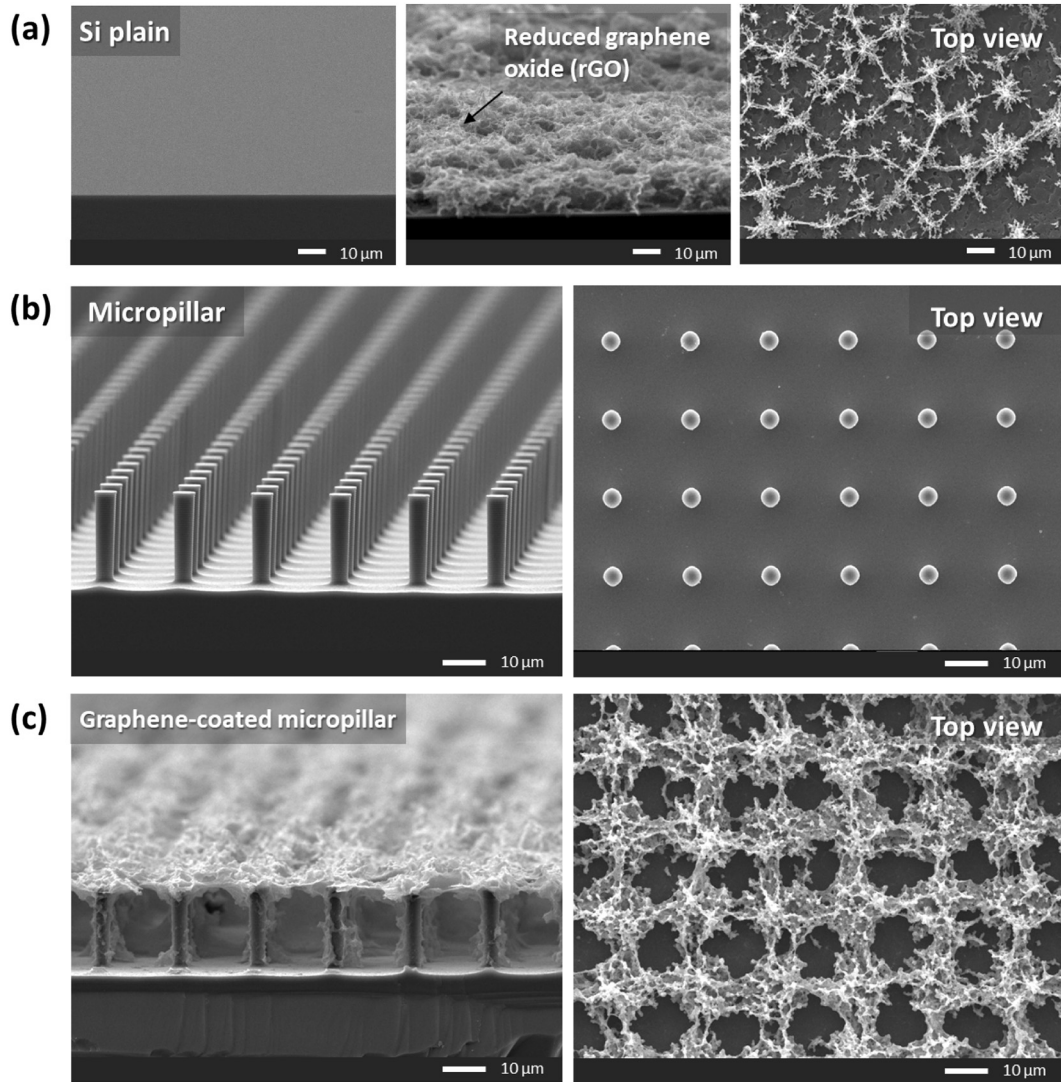
Fig. 4. Reduced graphene oxide (rGO) coated surfaces. (a) the SEM images of bare Si plain surface, cross view of rGO coated plain surface, and top view of rGO coated plain surface, (b) the SEM images of micropillar surface, (c) the SEM images of graphene-coated micropillar surface.
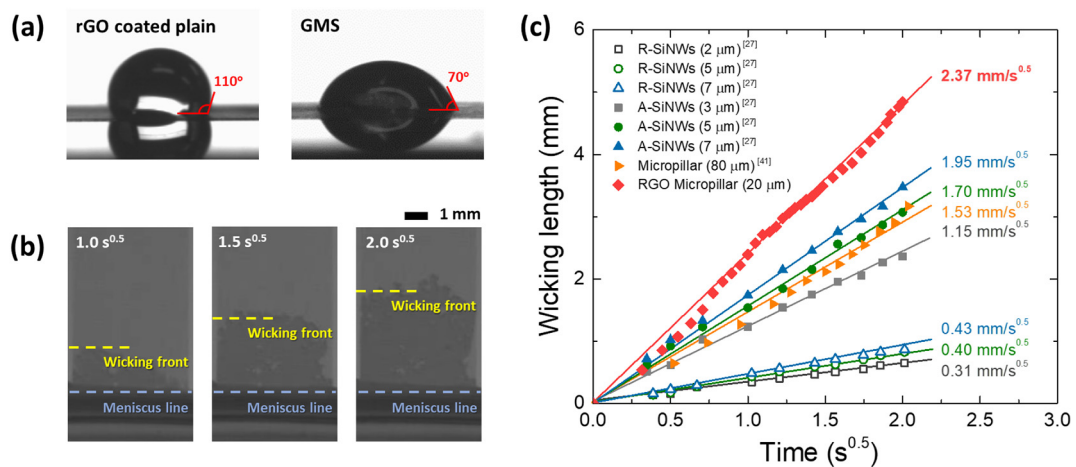

Fig. 5. Improved wicking performance by rGO coated micropillar, (a) Contact angle of the rGO coated plain and rGO coated micropillar surfaces, (b) Wicking images according to time. The blue dash line represents a meniscus line and the yellow dash line represents a dynamic wicking liquid front, (c) Wicking length vs. square root of time and wicking coefficient of micropillar, R-SiNWs and A-SiNWs. The wicking data of SiNWs and micropillar were taken from reference [27,41]. (For interpretation of the references to colour in this figure legend, the reader is referred to the web version of this article.)
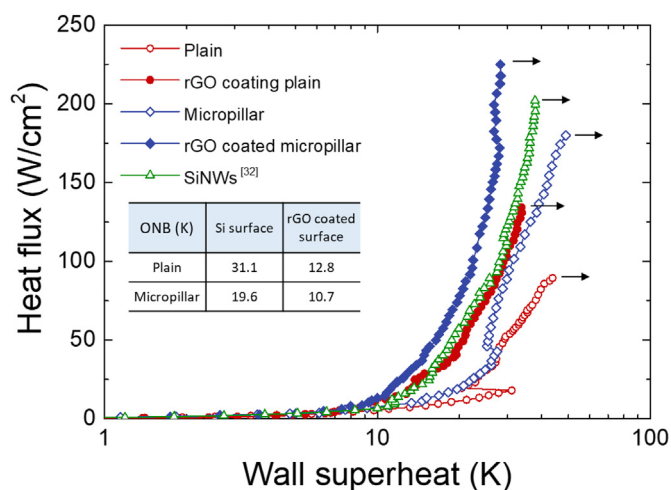
Fig. 6. Boiling characteristic curves according to rGO coating on micropillar. The inserted table is ONB of plain and micropillar surface according to the rGO coating.

material that is known to be hydrophobic. However, as shown in Fig. 5, the GMS surface has hydrophilicity with contact angle of 70° and excellent wicking properties. This is because the rGO particles contained in the GMS contain carboxylic acid groups, which belong to the hydrophilic functional group. Therefore, unlike standard hydrophobic graphene, the rGO particles of GMS are hydrophilic. As a result, the GMS surface has a high wicking rate of 2.37 mm/s$^{0.5}$.

3.2. Boiling heat transfer on the GMS surface

Fig. 6 shows the experimental results related to the boiling characteristics of rGO coatings on plain and micropillar surfaces. The circular symbols indicate the effect of the rGO coating on the plain surface, and the diamond symbols show the effect of the rGO coating on the micropillar surface. The triangles represent the boiling heat transfer characteristics of the nanowire surfaces described in previous studies. First, on the plain surface, the boiling curve moves to the left as rGO is coated on the surface, and the lower-wall temperature is maintained under the same heat flux condition. On the micropillar surface, wicking occurs through microstructures and stable nucleate boiling is possible up to higher heat flux conditions, so it exhibits a high CHF compared to that of the plain surface. The effect of surface-temperature reduction was also observed on the micropillar surface by using rGO coating. The nucleation-promotion effect of rGO coating causes a shift to the left in the boiling curve for both the plain and micropillar surfaces. It can be seen that the onset of nucleate boiling (ONB) at the rGO coating occurs at a lower wall temperature, as shown in the inserted table in Fig. 6. With the rGO coating, the ONB of the plain surface decreased from 31.1 K to 12.8 K, and the ONB of the micropillar surface decreased from 19.6 K to 10.7 K.

The coated rGO particles form a porous structure on the plain surface and the tip surface of the micropillar, as shown in the left-hand images of Fig. 7(a) and (b). The rGO porous structure contains cavities of several micrometers, a suitable size for generating the bubble nucleus.[32,42] Moreover, the high thermal conductivity of rGO transfers heat to the cavity in order to assist the growth of the bubble nucleus into a bubble. These characteristics of the rGO coating layer allow the initiation of nucleate boiling at low thermal energy, and the ONB is lowered on the rGO coating surface. The active nucleate boiling effect of the rGO coating layer can be clearly confirmed by bubble visualization, as shown in Fig. 7. Fig. 7(a) and (b) show the bubble visualization results for increasing heat flux at the micropillar and GMS surfaces, respectively. On the micropillar surface, one bubble is generated at the center of the heater. The number of nucleate sites did not

significantly increase with increasing heat flux, although the departure frequency and bubble diameter did increase (Supplementary Video clip). The surface of such a top and bottom of micropillar is smooth as shown in the Fig. 4(b), and the bubble is easily expanded larger than 10 mm until it covers all of the heater. During the bubble growth process, the boundary of bubble where most of the heat transfer occurs extends to the heater edge and shrinks when the bubble is departed. As the boundary of bubble sweeps across the heater, the heat of the whole heater area is removed during a bubble growth and departure cycle. Therefore, additional nucleate sites are less likely to occur and one or two nucleate sites are maintained in the high heat flux region on the micropillar surface. However, in the case of the GMS surface, small bubbles appear at several nucleate sites. The GMS surface contains numerous cavities in porous graphene layer that are suitable for nuclear boiling, and even low levels of thermal energy can initiate nucleation. The bubbles generated in the porous graphene structure is confined to a cavity-like structure due to the high roughness of graphene. The confined boundary of bubble generates small size bubbles based on the relation between surface tension and buoyancy force for bubble departure [43,44]. As the boundary of bubble is confined and only the heat of the local region is removed, the surrounding heater surface is superheated and new nucleate sites are activated. As nucleate boiling develops, the GMS surface generates many more active bubbles than the micropillar surface at the same heat flux condition (20 W/cm^2). In the high heat flux condition, the GMS surface maintains the bubble characteristics that occur at several nucleation sites, with a high frequency of small bubbles. The ripple in the bubble surface that is shown in Fig. 7(b) is generated by a capillary wave created during the merging of small bubbles on GMS surface. The small and fast bubble departure that is characteristic of the GMS surface facilitates liquid supply between bubbles and delays vapor film formation. By contrast, the single large bubble that is generated on the micropillar surface has a smooth surface.

Bubble characteristics in which small bubbles are quickly departed prevent the surface from overheating and help to maintain a low surface temperature. Here, the rGO coating layer activates nucleate boiling, and active nucleation increased the amount of heat removed per unit area, consequently improving the heat transfer coefficient (HTC). Fig. 8 shows the distributions of HTC for rGO coatings on plain and micropillar surfaces, respectively. The rGO coating increased the HTC across the entire boiling range and increased the maximum HTC by 96% on the plain surface and 114% on the micropillar surface. On the micropillar surface, the improvements in the HTC seems to be maximized because the vapor and liquid flow regions are divided by the rGO coating and micropillar layers. This structural design also improved the CHF, as shown in Fig. 9. As in previous studies, the CHF is strongly influenced by the wicking performance of the liquid supply in the vicinity of the bubble [27]. The micropillar surface exhibits a high CHF of 179 W/cm^2 due to its excellent wicking performance. However, due to the structure of the micropillar surface, which is not suitable for nucleate boiling, large bubble nucleation occurs at one or two sites. In comparison, the GMS surface presents both wicking performance due to the micropillar structure and a nucleate boiling effect due to the presence of rGO particles. The rGO porous structure has a cavity size of 2–3 μm, suitable for nucleate boiling, and bubble nucleation is activated with low thermal energy. In addition, the rGO layer has a mesh shape connected to the tip of the micropillar, so that the cooling fluid can easily be supplied to the micropillar layer through the spaces in the rGO mesh. The separation of vapor and liquid regions also prevents bubble trap and vapor film formation, even under high heat flux conditions. Thus, the wicking effect of the micropillar structure is further improved. As a result, the GMS significantly improves the heat transfer coefficient and CHF by 288% and 152%, respectively, compared to the plain surface. In addition, the excellent heat transfer characteristic of the GMS was evaluated over one day and the durability of GMS was confirmed as presented in the supporting information. These results can
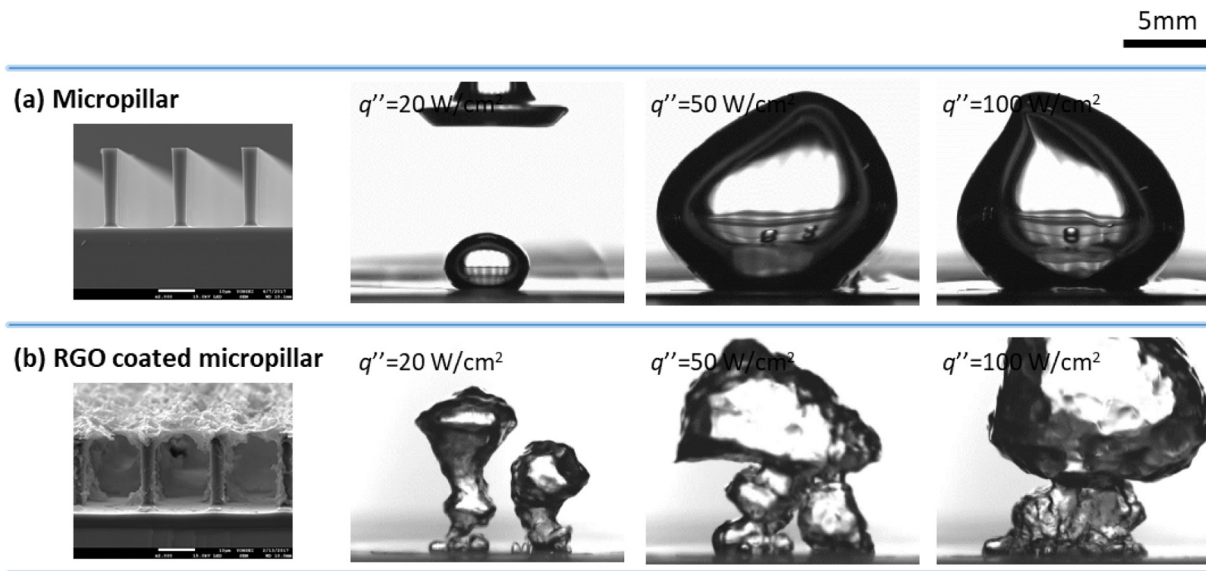
Fig. 7. Active bubble nucleation by RGO coating. (a) Bubble visualization of micropillar array surface, (b) Bubble visualization of RGO coated micropillar array surface.
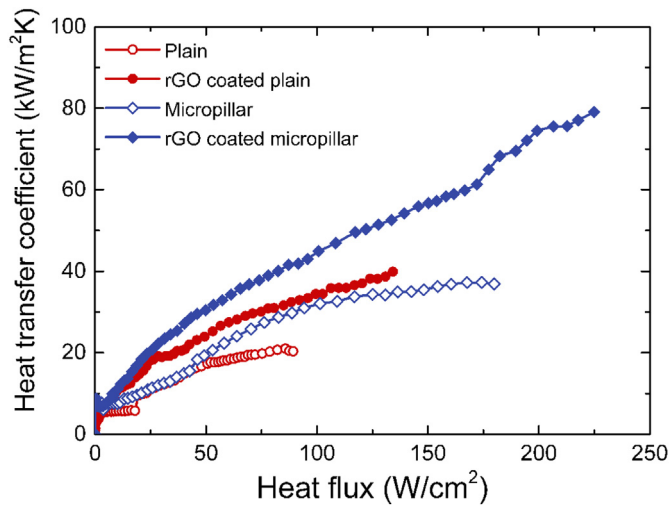

Fig. 8. Distributions of heat transfer coefficients on the plain and micropillar array surface according to RGO coating.
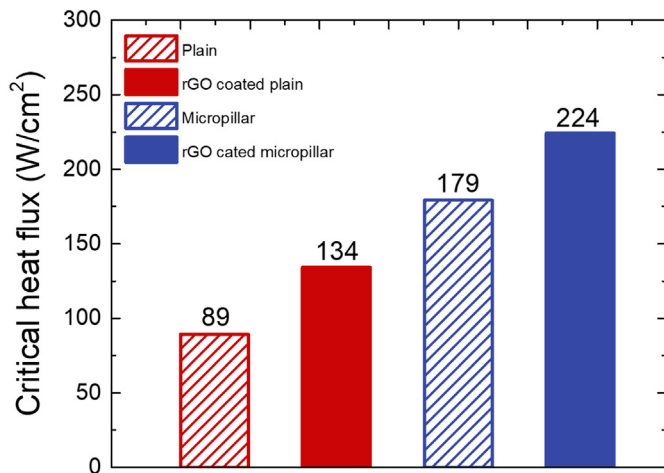

Fig. 9. Enhanced critical heat flux (CHF) by separated bubble nucleation region of liquid supply region.

be used in the field of extreme cooling and applied to processes that employ boiling heat transfer, such as computer chip cooling, heat exchanger, and nuclear-reactor.

4. Conclusions

In this study, we proposed a rGO-coated micropillar structure (GMS) surface that is able to separate bubble nucleation and liquid supply regions. In particular, the rGO porous structure facilitated bubble nucleation by providing a suitably sized cavity. A micropillar array with excellent wicking performance is located below the rGO porous layer in order to prevent bubble trap by providing a liquid beneath the vapor bubbles. As a result, vapor film formation is reduced in the GMS and boiling heat transfer performance is maximized. Moreover, the heat transfer coefficient and the critical heat flux are increased by 288% and 152%, respectively, when compared to the plain surface. In our future studies, we will aim to improve boiling performance by controlling the bubble nucleation sites on the GMS surface in order to further enhancing the CHF.

Supplementary data to this article can be found online at https://doi.org/10.1016/j.icheatmasstransfer.2019.104331.

Author contributions

The conceptual idea of this study was established by G. Choi, D.I. Shim, D. Lee, B.S. Kim and H.H.Cho. G. Choi and D.I. Shim fabricated the materials and G. Choi, D.I. Shim, B.S. Kim conducted boiling experiments. G. Choi and D. Lee recorded bubble visualization and all authors analyzed results and wrote the paper. H. H.Cho supervised the project.

References

[1] H. Kim, Enhancement of critical heat flux in nucleate boiling of nanofluids: a state-of-art review, Nanoscale Res. Lett. 6 (1) (2011) 415.

[2] N. Zuber, Hydrodynamic Aspects of Boiling Heat Transfer, PhD thesis, AECU-4439 University of California, Los Angeles, United States, 1959.

[3] Y. Katto, Y. Haramura, A new hydrodynamic model of critical heat flux applicable widely to both pool and forced convection boiling on submerged bodies in saturated liquids, Int. J. Heat Mass Transf. 26 (3) (1983) 389–399.

[4] N.S. Dhillon, J. Buongiorno, K.K. Varanasi, Critical heat flux maxima during boiling crisis on textured surfaces, Nat. Commun. 6 (2015) 8247.

[5] W.M. Rohsenow, P. Griffith, Correlation of Maximum Heat Flux Data for Boiling of Saturated Liquids, Massachusetts Institute of Technology, Division of Industrial Cooperation, Cambridge, Mass, 1955.

[6] J. Linehard, V.K. Dhir, Extended hydrodynamic theory of the peak and minimum pool boiling heat fluxes, NASA Contractor Reports, NASA CR-2270, 1973.

[7] S.M. You, J.H. Kim, K.H. Kim, Effect of nanoparticles on critical heat flux of water in pool boiling heat transfer, Appl. Phys. Lett. 83 (16) (2003) 3374–3376.

[8] S. Yao, X. Huang, Y. Song, Y. Shen, S. Zhang, Effects of nanoparticle types and size on boiling feat transfer performance under different pressures, AIP Adv. 8 (2) (2018) 025005.

[9] S. Zeinali Heris, S.G. Etemad, M. Nasr Esfahany, Experimental investigation of oxide nanofluids laminar flow convective heat transfer, Int. Commun. Heat Mass Transf. 33 (4) (2006) 529–535.

[10] F. Rostamian, N. Etesami, Pool boiling characteristics of silica/water nanofluid and variation of heater surface roughness in domain of time, Int. Commun. Heat Mass Transfer 95 (2018) 98–105.

[11] P. Naphon, C. Thongjing, Pool boiling heat transfer characteristics of refrigerant-nanoparticle mixtures, Int. Commun. Heat Mass Transfer 52 (2014) 84–89.

[12] S.M. Kwark, R. Kumar, G. Moreno, J. Yoo, S.M. You, Pool boiling characteristics of low concentration nanofluids, Int. J. Heat Mass Transf. 53 (5–6) (2010) 972–981.

[13] S.K. Gupta, R.D. Misra, Experimental study of pool boiling heat transfer on copper surfaces with Cu-Al2O3 nanocomposite coatings, Int. Commun. Heat Mass Transf. 97 (2018) 47–55.

[14] S.D. Park, S. Won Lee, S. Kang, I.C. Bang, J.H. Kim, H.S. Shin, D.W. Lee, D. Won Lee, Effects of nanofluids containing graphene/graphene-oxide nanosheets on critical heat flux, Appl. Phys. Lett. 97 (2) (2010) 023103.

[15] H.S. Ahn, J.M. Kim, C. Park, J.W. Jang, J.S. Lee, H. Kim, M. Kaviany, M.H. Kim, A novel role of three dimensional graphene foam to prevent heater failure during boiling, Sci. Rep. 3 (2013) 1960.

[16] H. Seo, J.H. Chu, S.-Y. Kwon, I.C. Bang, Pool boiling CHF of reduced graphene oxide, graphene, and SiC-coated surfaces under highly wettable FC-72, Int. J. Heat Mass Transfer 82 (2015) 490–502.

[17] M.S. Kamel, F. Lezsovits, A.M. Hussein, O. Mahian, S. Wongwises, Latest developments in boiling critical heat flux using nanofluids: a concise review, Int. Commun. Heat Mass Transf. 98 (2018) 59–66.

[18] H.S. Ahn, J.M. Kim, J.M. Kim, S.C. Park, K. Hwang, H.J. Jo, T. Kim, D.W. Jerng, M. Kaviany, M.H. Kim, Boiling characteristics on the reduced graphene oxide films, Exp. Ther. Fluid Sci. 60 (2015) 361–366.

[19] C.-C. Hsu, P.-H. Chen, Surface wettability effects on critical heat flux of boiling heat transfer using nanoparticle coatings, Int. J. Heat Mass Transf. 55 (13–14) (2012) 3713–3723.

[20] S.G. Kandlikar, A theoretical model to predict Pool boiling CHF incorporating effects of contact angle and orientation, J. Heat Transfer 123 (6) (2001) 1071.

[21] R. Chen, M.-C. Lu, V. Srinivasan, Z. Wang, H.H. Cho, A. Majumdar, Nanowires for enhanced boiling heat transfer, Nano Lett. 9 (2009) 548–553.

[22] K.K. Lay, J.S. Ong, K.Y. Yong, M.K. Tan, Y.M. Hung, Nucleate pool boiling enhancement by ultrafast water permeation in graphene-nanostructure, Int. Commun. Heat Mass Transfer 101 (2019) 26–34.

[23] E.W. Washburn, The dynamics of capillary flow, Phys. Rev. 17 (3) (1921) 273–283.

[24] M.M. Rahman, E. Olceroglu, M. McCarthy, Role of wickability on the critical heat flux of structured superhydrophilic surfaces, Langmuir 30 (37) (2014) 11225–11234.

[25] S. Shin, G. Choi, B. Rallabandi, D. Lee, D.I. Shim, B.S. Kim, K.M. Kim, H.H. Cho, Enhanced boiling heat transfer using self-actuated Nanobimorphs, Nano Lett. 18 (10) (2018) 6392–6396.

[26] B.S. Kim, H. Lee, S. Shin, G. Choi, H.H. Cho, Interfacial wicking dynamics and its impact on critical heat flux of boiling heat transfer, Appl. Phys. Lett. 105 (19) (2014) 191601.

[27] D.I. Shim, G. Choi, N. Lee, T. Kim, B.S. Kim, H.H. Cho, Enhancement of Pool boiling heat transfer using aligned silicon nanowire arrays, ACS Appl. Mater. Interfaces 9 (20) (2017) 17595–17602.

[28] B.S. Kim, B.I. Lee, N. Lee, G. Choi, T. Gemming, H.H. Cho, Nano-inspired smart interfaces: fluidic interactivity and its impact on heat transfer, Sci. Rep. 7 (2017) 45323.

[29] B.S. Kim, G. Choi, D.I. Shim, K.M. Kim, H.H. Cho, Surface roughening for hemi-wicking and its impact on convective boiling heat transfer, Int. J. Heat Mass Transf. 102 (2016) 1100–1107.

[30] J.M. Kim, S.C. Park, B. Kong, H.-B.-R. Lee, H.S. Ahn, Effect of porous graphene networks and micropillar arrays on boiling heat transfer performance, Exp. Thermal Fluid Sci. 93 (2018) 153–164.

[31] J.P. McHale, S.V. Garimella, T.S. Fisher, G.A. Powell, Pool boiling performance comparison of smooth and sintered copper surfaces with and without carbon na-notubes, Nanoscale Microscale Thermophysical Eng. 15 (3) (2011) 133–150.

[32] B.S. Kim, S. Shin, D. Lee, G. Choi, H. Lee, K.M. Kim, H.H. Cho, Stable and uniform heat dissipation by nucleate-catalytic nanowires for boiling heat transfer, Int. J. Heat Mass Transf. 70 (2014) 23–32.

[33] W.S. Hummers, R.E. Offeman, Preparation of graphitic oxide, J. Am. Chem. Soc. 80 (6) (1958) (1339–1339).

[34] D. Li, M.B. Muller, S. Gilje, R.B. Kaner, G.G. Wallace, Processable aqueous dispersions of graphene nanosheets, Nat. Nanotechnol. 3 (2) (2008) 101–105.

[35] S.H. Tamboli, B.S. Kim, G. Choi, H. Lee, D. Lee, U.M. Patil, J. Lim, S.B. Kulkarni, S. Chan Jun, H.H. Cho, Post-heating effects on the physical and electrochemical capacitive properties of reduced graphene oxide paper, J. Mater. Chem. A 2 (14) (2014) 5077–5086.

[36] D. Lee, B.S. Kim, H. Moon, N. Lee, S. Shin, H.H. Cho, Enhanced boiling heat transfer on nanowire-forested surfaces under subcooling conditions, Int. J. Heat Mass Transf. 120 (2018) 1020–1030.

[37] D. Lee, J.-S. Lim, L. Lee, H.H. Cho, Enhanced thermal uniformity and stability in pool boiling heat transfer using ultrasonic actuation, Int. Commun. Heat Mass Transfer 106 (2019) 22–30 (Accepted).

[38] S.J. Kim, I.C. Bang, J. Buongiorno, L.W. Hu, Surface wettability change during pool boiling of nanofluids and its effect on critical heat flux, Int. J. Heat Mass Transf. 50 (19–20) (2007) 4105–4116.

[39] D.E. Kim, D.I. Yu, S.C. Park, H.J. Kwak, H.S. Ahn, Critical heat flux triggering mechanism on micro-structured surfaces: coalesced bubble departure frequency and liquid furnishing capability, Int. J. Heat Mass Transf. 91 (2015) 1237–1247.

[40] D.I. Yu, H.J. Kwak, H. Noh, H.S. Park, K. Fezzaa, M.H. Kim, Synchrotron x-ray imaging visualization study of capillary-induced flow and critical heat flux on surfaces with engineered micropillars, Sci. Adv. 4 (2) (2018) e1701571.

[41] B. Darbois Texier, P. Laurent, S. Stoukatch, S. Dorbolo, Wicking through a confined micropillar array, Microfluid. Nanofluid. 20 (4) (2016) 53.

[42] Y.Y. Hsu, On the size range of active nucleation cavities on a heating surface, J. Heat Transf. 84 (1962) 207–213.

[43] W. Sluyter, P. Slooten, C. Copraij, A. Chesters, The departure size of pool-boiling bubbles from artificial cavities at moderate and high pressures, Int. J. Multiphase Flow 17 (1) (1991) 153–158.

[44] P.A. Raghupathi, S.G. Kandlikar, Pool boiling enhancement through contact line augmentation, Appl. Phys. Lett. 110 (2017) 204101.